

# Spatial and Temporal Coherence in Strongly Coupled Plasmonic Bose–Einstein Condensates

Antti J. Moilanen,<sup>1</sup> Konstantinos S. Daskalakis,<sup>1,2</sup> Jani M. Taskinen,<sup>1</sup> and Päivi Törmä<sup>1,\*</sup>

<sup>1</sup>*Department of Applied Physics, Aalto University School of Science, P.O. Box 15100, Aalto, FI-00076, Finland*

<sup>2</sup>*Department of Mechanical and Materials Engineering,*

*Turku University Faculty of Technology, Turku, FI-20014, Finland*

(Dated: March 1, 2025)

We report first-order spatial and temporal correlations in strongly coupled plasmonic Bose–Einstein condensates. The condensate is large, more than twenty times the intrinsic spatial coherence length of the polaritons and hundred times the healing length, making plasmonic lattices an attractive platform for studying long-range spatial correlations in two dimensions. We find that both spatial and temporal coherence display non-exponential decay; the results suggest power-law or stretched exponential behaviour with different exponents for spatial and temporal correlation decays.

Three-dimensional Bose-Einstein condensates (BECs) in thermal equilibrium exhibit long-range order of spatial correlations which, in principle, extend to infinity. In two dimensions, true long-range order is prohibited by thermal fluctuations [1–3]. Nevertheless, it has been shown that quasi-long-range order may persist in equilibrium systems through the Berezinskii–Kosterlitz–Thouless (BKT) transition [4, 5], and in non-equilibrium via the dynamical phase ordering of Kardar–Parisi–Zhang (KPZ) [6]. Exciton-polaritons (photon–exciton quasi-particles) offer a platform for studying correlations of driven-dissipative condensates in two dimensions, yet the occurrence of long-range order in these systems has remained elusive. Typically the systems have been too small to give definitive answers about decay at long distances. We introduce strongly coupled plasmonic BECs as a system for studying correlations: here we demonstrate a condensate of size more than twenty times the intrinsic spatial coherence of the polaritons and two orders of magnitude larger than the healing length, while in previous luminous condensates used for coherence studies the ratio of system size to intrinsic length scales has been approximately a factor of ten at best [7–10]. We find decay of spatial and temporal coherence that is clearly non-exponential; the results are best described by power-law or stretched exponential decay with different exponents for spatial and temporal correlations.

Various scenarios of long-range correlation decay have been predicted for two-dimensional systems. In equilibrium BECs, thermal fluctuations give rise to vortices and anti-vortices which disrupt the long-range ordering of correlations. In the BKT transition, below a critical temperature, vortices and anti-vortices are paired such that their phases cancel out allowing algebraic decay of correlations,  $g^{(1)}(x) \propto x^{-b}$ . The BKT transition entails power-law decays of both spatial and temporal correlations with equal exponents  $b_s = b_t \leq 0.25$  [11], although it has been suggested that in the presence

of drive and dissipation the exponents may differ as  $b_s = 2b_t$  [12, 13]. In non-equilibrium condensates, the occurrence of the BKT transition has been theoretically both supported [12, 14] and refuted [15]. Long-range phase ordering could be restored by the KPZ mechanism with correlation decay scaling as a stretched exponential rather than power law [15–17]. A crossover between the KPZ dynamics and equilibrium-like BKT has been proposed, determined by the degree of anisotropy in the system [15, 18]. Contrary to BEC, for a usual laser an exponential decay of temporal correlations is expected [19].

Semiconductor polariton condensates [20–22] are typically far from equilibrium conditions due to the short lifetime of polaritons with respect to their thermalization time, however, a quasi-equilibrium state can be achieved by a dynamical balance of pump and dissipation [23, 24], and near equilibrium conditions are also possible [7, 25]. Polaritons decay via emission of photons, providing direct access to the properties of the condensate by standard optical techniques. This makes polariton condensates an attractive platform for studying spatial and temporal correlations. Early reports on spatial correlations in microcavity polariton condensates indicated algebraic decay [26, 27], whereas temporal correlations have been shown to decay as an exponential or a Gaussian [8, 28–32]. There have been very few studies governing both spatial and temporal correlations, thus the question of whether true long-range order exists in non-equilibrium polariton condensates remains open. At equilibrium-like conditions, with polariton lifetime exceeding the other characteristic timescales of the system, a BKT transition has been suggested with both spatial and temporal correlations showing a power-law decay with an exponent below 0.25 [7]. In general, establishing power-law behaviour quantitatively is challenging [33].

Spatial and temporal correlations have also been studied in other types of luminous condensates. In photon BECs [9, 10] and plasmonic polariton condensates (polariton lasers) [34] the correlations have shown exponen-

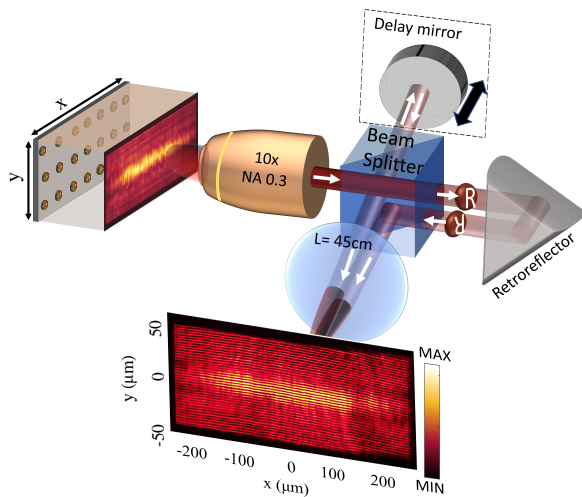


FIG. 1. Schematic of the experiment. An array of gold nanoparticles combined with a solution of fluorescent molecules is excited with a pulsed laser. The sample luminescence is imaged through a 10x microscope (NA 0.3) to a Michelson interferometer, which includes a cube beam splitter, a retroreflector, a delay stage mirror, and an  $f = 450$  mm bi-convex lens ( $L$ ). The real space image is inverted over both  $x$  and  $y$  directions of the array and overlapped with the original image. The resulting interference fringe visibility is directly proportional to the first-order correlation function  $g^{(1)}$ .

tial and Gaussian decays; the absence of long-range order has been attributed to the small condensate size and finite-size effects [9] and to the presence of drive and dissipation [34]. Indeed, one of the central factors hindering the studies of long-range order in all types of polariton and photon condensates has been the small system size [15, 17].

Here, we introduce a plasmonic polariton BEC with long-range spatial correlations that extend to remarkably long distances [35]. We present the first thorough measurement and in-depth analysis of both the spatial and temporal coherence in plasmonic BECs. Our results clearly show that the correlations differ both from a non-ordered phase and from a laser. The exponents extracted from our data by power-law and stretched exponential fits hint to a scenario in between quasi-equilibrium and non-equilibrium.

*System and experiment.*—A schematic of the system and the experiment is presented in Fig. 1. Plasmonic lattices, comprising nanoparticle arrays covered with fluorescent molecules, have been used to create BECs in the weak [36] and strong [37] coupling regimes. Nanoparticle arrays give rise to surface lattice resonances (SLRs) which are hybrid modes of the localized surface plasmon resonances in the individual nanoparticles and light diffracted to the periodic array [38–40]. The  $\Gamma$ -point of the SLR dispersion provides a band edge for lasing [41, 42] and condensation [36, 37]. To study spatial correlation decay at long distances, we use structures similar to those in

our previous work [37], but extend the system size in  $x$  to  $500\mu\text{m}$  while keeping the  $y$  dimension at  $100\mu\text{m}$ . The arrays are covered with an 80 mM solution of IR-792 dye leading to strong coupling between the molecules and the SLR modes [37]. The plasmon-exciton-polaritons, called polaritons hereafter, in the system are bosonic quasi-particles consisting of light diffracted to the array, electron plasma oscillation, and the dye molecule excitons. The molecules are excited by a pulsed laser (50 fs, 1 kHz, 800 nm) with a spot larger than the arrays. See Supplemental Material [43] for descriptions of the sample fabrication and the experimental setup.

As in our previous work [37], upon increasing pump fluence, the samples exhibit a double threshold, where the first threshold corresponds to polariton lasing and the second threshold to polariton BEC (see Fig. 3(d)). Since the polariton lifetime  $\sim 100$  fs is of the same order as the other timescales of the system, it is reasonable to assume the condensate to be in quasi- or non-equilibrium regime. However, distinct from most polariton condensates, we observe a thermal distribution that extends over a range of  $2k_B T$  at room temperature (see Fig. S1 [43]).

We measure spatial and temporal coherence of the sample by a Michelson interferometer in a mirror-retroreflector configuration. The retroreflector inverts the real space image centrosymmetrically i.e. in both  $x$  and  $y$  directions of the array. The inverted and non-inverted images are overlapped at a CMOS camera, and the combined image shows interference fringes when the light emitted by the sample is coherent. The fringe contrast is directly proportional to the first-order correlation function between two points separated by  $|\mathbf{r} - \mathbf{r}'|$ ,  $g^{(1)}(\mathbf{r}, \mathbf{r}'; \tau)$ , where  $\tau$  is the time delay between the two arms of the interferometer. Thus, changing the longitudinal position of the delay mirror and recording interferograms over a range of delays allows for directly probing the temporal coherence of the sample. For spatial coherence, we measure a series of interferograms at fixed intervals around zero time-delay,  $\tau = 0$ , over three periods of light frequency oscillation. The interferograms are normalized with images taken separately from each arm by blocking one arm at time. Finally, the first-order correlation function is obtained by fitting a sinusoidal function through each pixel of the stack of normalized interferograms, providing the amplitude and phase of the interference fringes; see [43] for details of the analysis.

*Spatial coherence.*—Figure 2 shows interferograms, the corresponding  $g^{(1)}(\mathbf{r}, -\mathbf{r}; \tau = 0)$  maps, and average  $g^{(1)}(x)$  along the long axis of the lattice for three excitation regimes: below, at, and above BEC threshold. The maps of the phase of the fringes are presented in Fig. S3 [43]. Below the threshold, spatial coherence emerges around the center of the array and decays towards the edges. At the threshold, coherence extends over a longer distance but gradual decay is still visible. Remarkably, above the threshold, coherence is nearly

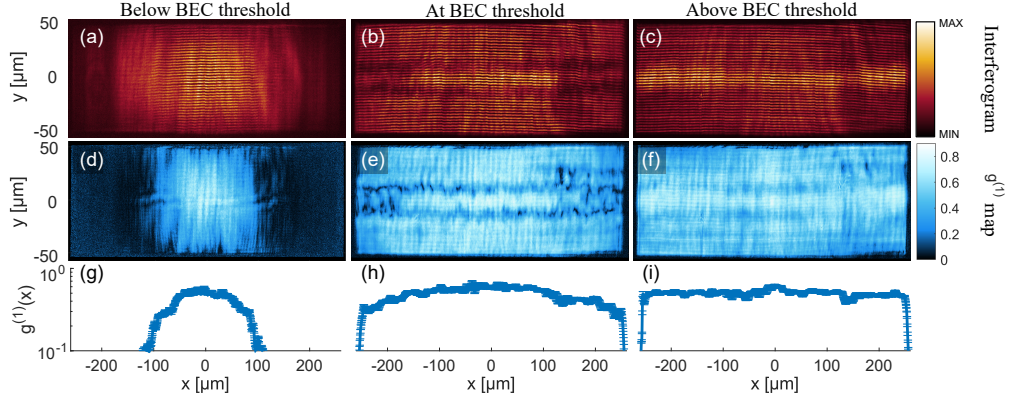


FIG. 2. Interferograms and spatial correlation maps. Interferograms at three pump fluences (a) below ( $0.83 \text{ mJcm}^{-2}$ ), (b) at ( $1.66 \text{ mJcm}^{-2}$ ), and (c) above ( $3.31 \text{ mJcm}^{-2}$ ) the BEC threshold. (d-f) Maps of  $g^{(1)}(\mathbf{r}, -\mathbf{r})$  for the corresponding pump fluences. (g-i) Average  $g^{(1)}(x)$  over the  $y$ -axis of the array. The error bars show the standard deviation of three measurements.

constant throughout the array.

Let us have a closer look at the decay of correlations. Fig. 3(a-c) show  $g^{(1)}$  as a function of radial separation of centrosymmetric points,  $\Delta r = |\mathbf{r} - \mathbf{r}'|$ , for the pump fluences highlighted with filled symbols in Fig. 3(d). The measured  $g^{(1)}(\Delta r)$  are fit to Gaussian, exponential, stretched exponential, and power-law functions:

$$g^{(1)}(\Delta r) = ae^{-(\Delta r/d)^\beta}, \quad (1)$$

$$g^{(1)}(\Delta r) = a\Delta r^{-b}, \quad (2)$$

where  $\beta = 2$  gives a Gaussian and  $\beta = 1$  an exponential function, and  $0 < a \leq 1$  is a scaling parameter. Note that power-law or stretched exponential behaviour are expected to occur only above the threshold fluence for the BEC transition. We exclude the short-range regime around the autocorrelation point ( $\Delta r = 0$ ) from the fits, determined by the spatial coherence length of the polaritons without pumping,  $24 \mu\text{m}$  [37]. All the fits are performed using the same fit range, and the best-fitting model is shown in Fig. 3(a-c) for each case. At pump fluences below the BEC threshold, as shown in Fig. 3(a-b), spatial correlations decay as a Gaussian. Above the threshold, Fig. 3(c), long-range spatial coherence covering the entire array emerges and the correlation function is nearly constant over a remarkably long distance: a fit to an exponential function yields a correlation decay length of  $3235 \mu\text{m}$ , which is more than six times the long axis of the system, and *two orders of magnitude* larger than the intrinsic coherence length of the polaritons. The decay lengths as given by Gaussian and exponential fits are presented in Fig. 3(d) alongside the threshold curve. However, the data is best fit to a power-law function with a very small exponent of 0.07, and almost equally with a stretched exponential with an exponent of around 0.1. The fits to all four functions are presented in Fig. S6 [43]. Fig. 3(e-f) show the exponents obtained from the stretched exponential and power-law

fits above the BEC transition. The root-mean-square error (RMSE) of the fits are compared in Fig. 3(g).

That the spatial coherence extends to such large distances over the lattice in  $x$  direction is non-trivial con-

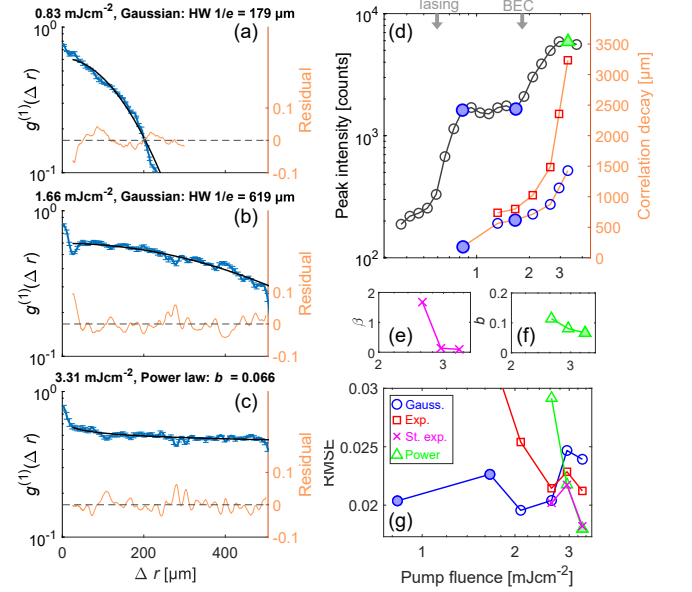


FIG. 3. Quantitative analysis of spatial correlation decay. Measured  $g^{(1)}(\Delta r)$  at three pump fluences (a) below, (b) at, and (c) above the BEC threshold. The error bars represent the standard deviation of three measurements. The best-fitting functions are shown by black solid lines. (d) Threshold curve (black circles) and spatial correlation decay extracted from Gaussian (blue circles) and exponential fits (red squares). The fluences corresponding to (a-c) are highlighted with filled circles and the green triangle. For the exponential function, the reported length is the decay constant and for the Gaussian the half width (HW) at  $1/e$  decay. Exponents extracted from (e) stretched exponential and (f) power-law fits. (g) RMSE of the fits. In (d-f) the horizontal axis values are the pump fluence in the same units as in (g).

sidering the intrinsic anisotropy of the process. The pump excites mainly the molecules but also weakly (off-resonantly) the nanoparticles: the nanoparticle excitations follow the pump polarization and stimulate emission from the molecules to SLR modes of the same polarization [43]. In the experiments reported here, the pump polarized linearly in  $x$  triggers propagation of high energy (high momentum  $\mathbf{k}$ ) polaritons in the  $y$  direction of the array. In the beginning of the thermalization process,  $y$  direction is thus favoured. Nevertheless, the BEC that forms around the band edge ( $\mathbf{k} = 0$ ) shows coherence in both  $x$  and  $y$ , in contrast to lasing at the first threshold which is coherent only in  $y$ . This qualitative change of spatial coherence from lasing to BEC was found already in our previous work [37], but for a sample of only 100  $\mu\text{m}$  size in  $x$  (coherence decay laws were not studied there, limited by the small sample size). The present observations of coherence in the  $x$  direction over a much longer distance corroborate the 2D nature of the BEC.

The thermalization in the plasmonic polariton BEC involves stimulated processes enabling an ultrafast time scale in which the condensate is formed ( $< 250$  fs) [37]. Here, we separated the thermal tail (the part of the BEC spectrum which displays the Maxwell-Boltzmann distribution) of the condensate emission using band-pass filters and found that the thermal tail is coherent (Fig. S5 [43]). This confirms that the thermalization is a coherent process.

*Temporal coherence.*—Temporal coherence of the sample is measured over a longer delay range and with a coarser time step. Here, we extract the fringe contrast directly by fitting the fringes in the normalized interferograms to a sinusoidal function. The fringes are analyzed from 24  $\mu\text{m}$  wide rectangles around  $x = 0$ , and the  $g^{(1)}(\tau)$  obtained from all locations in the  $y$ -axis of the array are averaged. The averaging is necessary due to interference that arises from the counter-propagating polaritons along  $y$  [37] (see [43] and Fig. S7 for more information). Temporal coherence for increasing pump fluence is displayed in Fig. 4(d); the pump fluences are color-coded with respect to the threshold curve (inset). Similarly to the spatial analysis, the measured  $g^{(1)}(|\tau|)$  are fit to Gaussian, exponential, stretched exponential, and power-law functions, and the best-fitting models are shown in Fig. 4(a-c). The data corresponding to the short-range correlations, between  $\tau = 0$  and the SLR mode lifetime  $\tau = 100$  fs, are excluded from the fits. Below the BEC threshold, as shown in Fig. 4(a), correlations decay exponentially with a decay constant of 362 fs. This already exceeds the intrinsic temporal coherence of the plasmonic modes due to the lasing triggered at the first threshold. Above the BEC threshold, Fig. 4(b-c), the data is best fit to a power-law function with an exponent of around 0.7–0.8; the stretched exponential fits almost equally well with an exponent of  $\beta \sim 0.2$ , given by Fig. 4(e-f). Fig. 4(g) presents the comparison of the RMSE of the fits.

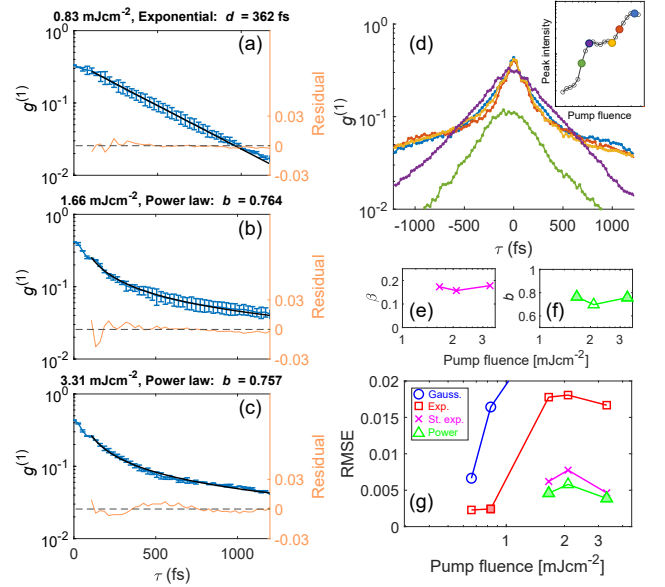


FIG. 4. Quantitative analysis of temporal correlation decay. (a-c) Measured  $g^{(1)}(|\tau|)$  at three pump fluences (a) below, (b) at, and (c) above the BEC threshold. The error bars represent the standard deviation of the averaged  $\tau < 0$  and  $\tau > 0$  values from (d). Fits to the best-fitting function are shown with black solid lines. (d) Measured temporal coherence for different pump fluences, color coded according to the filled circles in the threshold curve (inset). Exponents extracted from (e) stretched exponential and (f) power-law fits. (g) RMSE of the fits.

*Discussion.*—At pump fluences far below the BEC threshold but above the polariton lasing threshold, the system behaves much like a (regular or polariton) laser: spatial correlations decay as a Gaussian and temporal correlations as an exponential function. Nanoparticle array lasers at weak coupling regime have previously shown Gaussian decay of both spatial and temporal correlations [44], and at strong coupling an exponential decay of spatial and a quasi-Gaussian decay of temporal correlations [34]. In polariton condensates, temporal correlation decay has been reported to be Gaussian [8, 28–30, 45] or of Kubo form, that is, Gaussian or exponential depending on whether the number fluctuations are slow or fast [31, 32].

Above the BEC threshold, both spatial and temporal correlations show decay that indicates power-law behaviour. Spatial correlations decay with a small exponent of 0.07 whereas temporal correlations with a large exponent of around 0.7–0.8. This clearly differs from equilibrium BKT transition, as could be expected due to the driven-dissipative nature of our system. It is worthwhile to mention that we have also looked at few- and single-shot interferograms of the condensate and have not observed vortices. In driven-dissipative condensates, the power-law exponent may exceed the equilibrium BKT limit 0.25, but our findings do not directly match with



the previously reported experimental [26] or theoretical values [12, 14].

Stretched exponential function, related to KPZ dynamics, fits approximately equally well as the power law, yielding small exponents  $\beta$ . The KPZ scaling of spatial and temporal correlations has been mostly considered in the optical parametric oscillator (OPO) regime of microcavity polariton condensates [16, 18]. In the strongly anisotropic case, the KPZ equation leads to a power-law decay of spatial correlations with exponent  $b_s = 2\chi$ , where  $\chi$  is the roughness exponent that in two dimensions takes the universal value of 0.39 [46–48]. Likewise, the temporal correlations decay as power law but with exponent that is 1/2 of the spatial exponent,  $b_t = \chi$ . In the regime of weak anisotropy, the two-dimensional KPZ equation predicts a stretched exponential decay with  $\beta_s = 2\chi = 0.78$  for spatial and  $\beta_t = 2\chi/(2 - \chi) = 0.48$  for temporal correlations [18]. Our results yield  $\beta_s \approx 0.1$  and  $\beta_t \approx 0.2$  above the BEC threshold.

Our system is not isotropic. The nanoparticles host dipolar and multipolar charge oscillation modes associated with directional radiation, which combined with the periodicity of the array in the  $x$  and  $y$  directions leads to SLR modes that are not isotropic in the plane (in contrast to typical planar cavities). In an infinite or square array, there is still the  $x$ - $y$  symmetry left, but even this can be broken by the pump polarization as mentioned above. Evaluating the level of anisotropy in the sense of the theoretical predictions is difficult since our system is not analogous to those considered in Refs. [15, 18], however the KPZ scaling is expected to be rather universal.

Finally, it should be noted that the differences (e.g. RMSE) between fits of spatial and temporal correlations to different models have typically been marginal, and therefore establishing power-law behaviour quantitatively is not straightforward [7, 18, 26, 27]. Ideally the data should range over at least two decades to rigorously claim power-law behaviour [33]. The results depend on the fit range, so it is of key importance to justify the range (short vs. long-range) deliberately. Another notable feature is that the regime of pump powers where the transition to a BKT phase or KPZ dynamics is expected could be very narrow [12, 14, 17].

*Summary and outlook.*—We have characterized for the first time the spatial and temporal first-order correlations in a plasmonic BEC. We propose plasmonic lattice condensates as a platform for studying long-range order in two-dimensional condensates of light, with versatile system design and open cavity character. The combination of large size and short cavity lifetime makes the system amenable for probing non-equilibrium BKT transition or KPZ dynamics [15, 17, 18, 49]. In this work, we have shown that the decay of correlations above the BEC threshold is non-exponential, in stark contrast to the non-ordered and lasing phases. Our results indi-

cate algebraic decay of both spatial and temporal correlations with different exponents, however the stretched exponential fits approximately equally well. The exponents found do not quantitatively match with reported predictions for equilibrium or non-equilibrium systems. Although the scaling laws predicted by the equilibrium BKT and the non-equilibrium KPZ mechanisms might be universal, understanding the role of strongly coupled vibrational and electronic states, the ultrafast dynamics, and the type of anisotropy in plasmonic nanoparticle array condensates may bring in new physics and are important to consider in future theoretical work. On the experimental side, even larger samples could be studied, pump fluences probed with finer steps, and the sensitivity of the measurement increased in order to observe the decay of spatial correlations over a larger dynamic range of intensity, essential for distinguishing between power laws from other forms of decay.

Beyond fundamental studies of correlations, the plasmonic polariton BEC provides spatial coherence decay on the millimeter-scale, which is 1–2 orders of magnitude larger than in other polariton or photon condensates before. Millimeter-scale spatial coherence has been previously reported in weakly coupled plasmonic lasers [44]. Our strongly coupled plasmonic BEC provides also effective interactions [37], which may give rise to phenomena not accessible in weakly coupled and non-interacting systems, such as superfluidity [50]. The large extent of spatial coherence could be utilized in, for instance, on-chip applications for sensing, where lasing and condensation can make tiny effects observable, and in the far future also in information processing.

*Acknowledgments*— We thank Jonathan Keeling and Kristin B. Arnardottir for their comments on the early version of the manuscript. AJM and PT acknowledge support by the Academy of Finland under project numbers 303351, 307419, 327293, 318987 (QuantERA project RouTe), 318937 (PROFI), and by Centre for Quantum Engineering (CQE) at Aalto University. AJM acknowledges financial support by the Jenny and Antti Wihuri Foundation. KD acknowledges financial support from the European Research Council (ERC) under the European Union’s Horizon 2020 research and innovation programme (grant agreement No. [948260]).

---

\* paivi.torma@aalto.fi

- [1] N. D. Mermin and H. Wagner, *Absence of Ferromagnetism or Antiferromagnetism in One- or Two-Dimensional Isotropic Heisenberg Models*, Physical Review Letters **17**, 1133 (1966).
- [2] P. C. Hohenberg, *Existence of Long-Range Order in One and Two Dimensions*, Physical Review **158**, 383 (1967).
- [3] I. Bloch, J. Dalibard, and W. Zwerger, *Many-Body Physics with Ultracold Gases*, Reviews of Modern Physics

- 80**, 885 (2008).
- [4] J. M. Kosterlitz and D. J. Thouless, *Ordering, metastability and phase transitions in two-dimensional systems*, Journal of Physics C: Solid State Physics **6**, 1181 (1973).
  - [5] V. L. Berezinskii, *Destruction of Long-range Order in One-dimensional and Two-dimensional Systems having a Continuous Symmetry Group I. Classical Systems*, Soviet Physics JETP **32**, 493 (1971).
  - [6] M. Kardar, G. Parisi, and Y.-C. Zhang, *Dynamic Scaling of Growing Interfaces*, Physical Review Letters **56**, 889 (1986).
  - [7] D. Caputo, D. Ballarini, G. Dagvadorj, C. Sánchez Muñoz, M. De Giorgi, L. Dominici, K. West, L. N. Pfeiffer, G. Gigli, F. P. Laussy, M. H. Szymańska, and D. Sanvitto, *Topological order and thermal equilibrium in polariton condensates*, Nature Materials **17**, 145 (2018).
  - [8] K. Daskalakis, S. Maier, and S. Kéna-Cohen, *Spatial Coherence and Stability in a Disordered Organic Polariton Condensate*, Physical Review Letters **115**, 035301 (2015).
  - [9] T. Damm, D. Dung, F. Vewinger, M. Weitz, and J. Schmitt, *First-order spatial coherence measurements in a thermalized two-dimensional photonic quantum gas*, Nature Communications **8**, 158 (2017).
  - [10] J. Marelic, L. F. Zajiczek, H. J. Hesten, K. H. Leung, E. Y. X. Ong, F. Mintert, and R. A. Nyman, *Spatiotemporal coherence of non-equilibrium multimode photon condensates*, New Journal of Physics **18**, 103012 (2016).
  - [11] D. R. Nelson and J. M. Kosterlitz, *Universal Jump in the Superfluid Density of Two-Dimensional Superfluids*, Physical Review Letters **39**, 1201 (1977).
  - [12] P. Comaron, I. Carusotto, M. H. Szymanska, and N. P. Proukakis, *Non-equilibrium Berezinskii-Kosterlitz-Thouless transition in driven-dissipative condensates*, arXiv:2011.06365 [cond-mat] (2020).
  - [13] M. H. Szymańska, J. Keeling, and P. B. Littlewood, *Mean-field theory and fluctuation spectrum of a pumped decaying Bose-Fermi system across the quantum condensation transition*, Physical Review B **75**, 195331 (2007).
  - [14] G. Dagvadorj, J. Fellows, S. Matyjaśkiewicz, F. Marchetti, I. Carusotto, and M. Szymańska, *Nonequilibrium Phase Transition in a Two-Dimensional Driven Open Quantum System*, Physical Review X **5**, 041028 (2015).
  - [15] E. Altman, L. M. Sieberer, L. Chen, S. Diehl, and J. Toner, *Two-Dimensional Superfluidity of Exciton Polaritons Requires Strong Anisotropy*, Physical Review X **5**, 011017 (2015).
  - [16] A. Ferrier, A. Zamora, G. Dagvadorj, and M. H. Szymańska, *Searching for the Kardar-Parisi-Zhang phase in microcavity polaritons*, arXiv:2009.05177 [cond-mat] (2020).
  - [17] P. Comaron, G. Dagvadorj, A. Zamora, I. Carusotto, N. Proukakis, and M. Szymańska, *Dynamical Critical Exponents in Driven-Dissipative Quantum Systems*, Physical Review Letters **121**, 095302 (2018).
  - [18] A. Zamora, L. Sieberer, K. Dunnett, S. Diehl, and M. Szymańska, *Tuning across Universalities with a Driven Open Condensate*, Physical Review X **7**, 041006 (2017).
  - [19] A. L. Schawlow and C. H. Townes, *Infrared and Optical Masers*, Physical Review **112**, 1940 (1958).
  - [20] J. Kasprzak, M. Richard, S. Kundermann, A. Baas, P. Jeambrun, J. M. J. Keeling, F. M. Marchetti, M. H. Szymańska, R. André, J. L. Staehli, V. Savona, P. B. Littlewood, B. Deveaud, and L. S. Dang, *Bose-Einstein Condensation of Exciton Polaritons*, Nature **443**, 409 (2006).
  - [21] K. S. Daskalakis, S. A. Maier, R. Murray, and S. Kéna-Cohen, *Nonlinear Interactions in an Organic Polariton Condensate*, Nature Materials **13**, 271 (2014).
  - [22] J. D. Plumhof, T. Stöferle, L. Mai, U. Scherf, and R. F. Mahrt, *Room-Temperature Bose-Einstein Condensation of Cavity Exciton-Polaritons in a Polymer*, Nature Materials **13**, 247 (2014).
  - [23] I. Carusotto and C. Ciuti, *Quantum Fluids of Light*, Reviews of Modern Physics **85**, 299 (2013).
  - [24] J. Keeling and S. Kéna-Cohen, *Bose-Einstein Condensation of Exciton-Polaritons in Organic Microcavities*, Annual Review of Physical Chemistry **71**, 435 (2020).
  - [25] Y. Sun, P. Wen, Y. Yoon, G. Liu, M. Steger, L. N. Pfeiffer, K. West, D. W. Snoke, and K. A. Nelson, *Bose-Einstein Condensation of Long-Lifetime Polaritons in Thermal Equilibrium*, Physical Review Letters **118**, 016602 (2017).
  - [26] G. Roumpos, M. Lohse, W. H. Nitsche, J. Keeling, M. H. Szymańska, P. B. Littlewood, A. Löffler, S. Höfling, L. Worschech, A. Forchel, and Y. Yamamoto, *Power-law decay of the spatial correlation function in exciton-polariton condensates*, Proceedings of the National Academy of Sciences **109**, 6467 (2012).
  - [27] W. H. Nitsche, N. Y. Kim, G. Roumpos, C. Schneider, M. Kamp, S. Höfling, A. Forchel, and Y. Yamamoto, *Algebraic order and the Berezinskii-Kosterlitz-Thouless transition in an exciton-polariton gas*, Physical Review B **90**, 205430 (2014).
  - [28] F. Baboux, D. D. Bernardis, V. Goblot, V. N. Gladilin, C. Gomez, E. Galopin, L. L. Gratiet, A. Lemaître, I. Sagnes, I. Carusotto, M. Wouters, A. Amo, and J. Bloch, *Unstable and stable regimes of polariton condensation*, Optica **5**, 1163 (2018).
  - [29] A. P. D. Love, D. N. Krizhanovskii, D. M. Whittaker, R. Bouchekioua, D. Sanvitto, S. A. Rizeiqi, R. Bradley, M. S. Skolnick, P. R. Eastham, R. André, and L. S. Dang, *Intrinsic Decoherence Mechanisms in the Microcavity Polariton Condensate*, Physical Review Letters **101**, 067404 (2008).
  - [30] H. Haug, T. D. Doan, H. T. Cao, and D. B. T. Thoi, *Temporal first- and second-order correlations in a polariton condensate*, Physical Review B **85**, 205310 (2012).
  - [31] D. M. Whittaker and P. R. Eastham, *Coherence properties of the microcavity polariton condensate*, EPL (Europhysics Letters) **87**, 27002 (2009).
  - [32] R. Spano, J. Cuadra, C. Lingg, D. Sanvitto, M. D. Martin, P. R. Eastham, M. v. d. Poel, J. M. Hvam, and L. Viña, *Build up of off-diagonal long-range order in microcavity exciton-polaritons across the parametric threshold*, Optics Express **21**, 10792 (2013).
  - [33] A. Clauset, C. R. Shalizi, and M. E. J. Newman, *Power-Law Distributions in Empirical Data*, SIAM Review **51**, 661 (2009).
  - [34] M. De Giorgi, M. Ramezani, F. Todisco, A. Halpin, D. Caputo, A. Fieramosca, J. Gomez-Rivas, and D. Sanvitto, *Interaction and Coherence of a Plasmon-Exciton Polariton Condensate*, ACS Photonics **5**, 3666 (2018).
  - [35] The condensate size 500  $\mu\text{m}$  is more than 20 times the intrinsic spatial coherence length of the polaritons (24  $\mu\text{m}$ )

- and 100 times the healing length  $\xi_0 = \hbar/\sqrt{2m_{\text{eff}}gn}$ , calculated with values estimated for our system  $m_{\text{eff}} = 1e^{-7} - 1e^{-5}$  and  $gn = 0.02$  eV [37]. This gives a healing length between 0.6–6  $\mu\text{m}$ .
- [36] T. K. Hakala, A. J. Moilanen, A. I. Väkeväinen, R. Guo, J.-P. Martikainen, K. S. Daskalakis, H. T. Rekola, A. Julku, and P. Törmä, *Bose-Einstein Condensation in a Plasmonic Lattice*, *Nature Physics* **14**, 739 (2018).
  - [37] A. I. Väkeväinen, A. J. Moilanen, M. Nečada, T. K. Hakala, K. S. Daskalakis, and P. Törmä, *Sub-picosecond thermalization dynamics in condensation of strongly coupled lattice plasmons*, *Nature Communications* **11**, 3139 (2020).
  - [38] W. Wang, M. Ramezani, A. I. Väkeväinen, P. Törmä, J. G. Rivas, and T. W. Odom, *The Rich Photonic World of Plasmonic Nanoparticle Arrays*, *Materials Today* **21**, 303 (2018).
  - [39] V. G. Kravets, A. V. Kabashin, W. L. Barnes, and A. N. Grigorenko, *Plasmonic Surface Lattice Resonances: A Review of Properties and Applications*, *Chemical Reviews* **118**, 5912 (2018).
  - [40] D. Wang, W. Wang, M. P. Knudson, G. C. Schatz, and T. W. Odom, *Structural Engineering in Plasmon Nanolasers*, *Chemical Reviews* **118**, 2865 (2018).
  - [41] T. K. Hakala, H. T. Rekola, A. I. Väkeväinen, J.-P. Martikainen, M. Nečada, A. J. Moilanen, and P. Törmä, *Lasing in Dark and Bright Modes of a Finite-Sized Plasmonic Lattice*, *Nature Communications* **8**, 13687 (2017).
  - [42] K. S. Daskalakis, A. I. Väkeväinen, J.-P. Martikainen, T. K. Hakala, and P. Törmä, *Ultrafast Pulse Generation in an Organic Nanoparticle-Array Laser*, *Nano Letters* **18**, 2658 (2018).
  - [43] A. J. Moilanen, S. D. Konstantinos, J. M. Taskinen, and P. Törmä, *Supplemental Material* (2021), see Supplemental Material for detailed methodology and additional experiments.
  - [44] T. B. Hoang, G. M. Akselrod, A. Yang, T. W. Odom, and M. H. Mikkelsen, *Millimeter-Scale Spatial Coherence from a Plasmon Laser*, *Nano Letters* **17**, 6690 (2017).
  - [45] S. Kim, B. Zhang, Z. Wang, J. Fischer, S. Brodbeck, M. Kamp, C. Schneider, S. Höfling, and H. Deng, *Coherent Polariton Laser*, *Physical Review X* **6**, 011026 (2016).
  - [46] T. Halpin-Healy and G. Palasantzas, *Universal correlators and distributions as experimental signatures of (2+1)-dimensional Kardar-Parisi-Zhang growth*, *EPL (Europhysics Letters)* **105**, 50001 (2014).
  - [47] A. Pagnani and G. Parisi, *Numerical estimate of the Kardar-Parisi-Zhang universality class in (2+1) dimensions*, *Physical Review E* **92**, 010101 (2015).
  - [48] V. G. Miranda and F. D. A. Aarão Reis, *Numerical study of the Kardar-Parisi-Zhang equation*, *Physical Review E* **77**, 031134 (2008).
  - [49] L. He, L. M. Sieberer, E. Altman, and S. Diehl, *Scaling properties of one-dimensional driven-dissipative condensates*, *Physical Review B* **92**, 155307 (2015).
  - [50] J. Keeling, L. M. Sieberer, E. Altman, L. Chen, S. Diehl, and J. Toner, *Superfluidity and Phase Correlations of Driven Dissipative Condensates*, in *Universal Themes of Bose-Einstein Condensation* (Cambridge University Press, 2017) pp. 205–230, arXiv:1601.04495.
  - [51] P. B. Johnson and R. W. Christy, *Optical constants of noble metals*, *Phys. Rev. B* **6**, 4370 (1972).
  - [52] K. S. Daskalakis, *Room-temperature polariton condensates in all-dielectric microcavities*, Ph.D. thesis, Imperial College London (2014).
  - [53] M. Born and E. Wolf, *Principles of Optics* (Pergamon Press, Oxford, 1998).

**SUPPLEMENTAL MATERIAL FOR: “SPATIAL AND TEMPORAL COHERENCE IN STRONGLY COUPLED PLASMONIC BOSE-EINSTEIN CONDENSATES”**

**SAMPLES**

The nanoparticle arrays are fabricated on a glass substrate with electron beam lithography (EBL). A 2 nm adhesion layer of titanium and a 50 nm layer of gold are evaporated on a patterned poly(methyl methacrylate) layer on glass, followed by lift-off in acetone. Gold was chosen as the nanoparticle material because it is resistant to oxidation and has low losses in the near-infrared wavelengths where the experiments are conducted [51]. The arrays have asymmetric periodicities ( $p_y = 568$  nm,  $p_x = 618$  nm) and the cylindrical gold nanoparticles have a diameter of 105 nm and height of 50 nm. The asymmetric periods separate the dispersion of orthogonal polarizations, simplifying the data interpretation [37]. The nanoparticle arrays are covered with fluorescent dye IR-792 in a solution of 1:2 (dimethyl sulfoxide) : (benzyl alcohol). A large molecule reservoir (0.8 mm thick layer) helps the samples to sustain measurements for a long period of time because the dye can replenish between consecutive measurements.

The dye molecules are excited with a pulsed

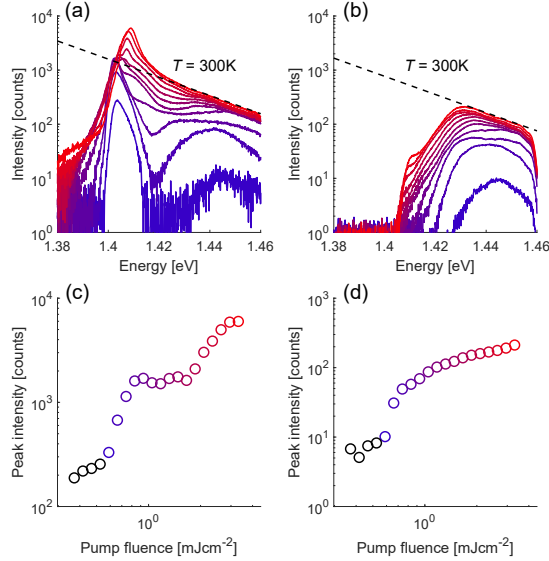


FIG. S1. Luminescence spectra as a function of pump fluence. Luminescence spectrum for (a) the whole spectrum and (b) the thermal cloud as a function of pump fluence. The pump fluences are color-coded from low (blue) to high (red) respective to (c) and (d), which show the threshold curves for the whole spectrum and the thermal cloud, respectively. Notably, the population of the thermal tail increases linearly as a function of pump fluence after the first threshold. At the second threshold this increase saturates and the population starts to accumulate to a peak around the band edge, in accordance with the BEC mechanism.

Ti:sapphire laser (50 fs, 1 kHz, 800 nm), the spot is cropped by an iris such that it has a diameter larger than the arrays and nearly flat-top intensity profile. The pump is horizontally polarized ( $x$  direction of the nanoparticle array). Even though the pump does not directly couple to the lattice modes (a pump beam at 800 nm and normal incidence is off-resonant with the SLR modes of our sample), a small spectral overlap of the pump and the single particle resonance (which is broad) excites the nanoparticles and causes the nanoparticle charge oscillations to be mainly polarized in  $x$ . Small nanoparticles act as dipole antennae, radiating mostly in the direction perpendicular to their polarization axis. This corresponds to an SLR mode with propagation along the  $y$ -axis of the lattice. The small pump-caused  $x$ -polarized excitation in the nanoparticles stimulates  $x$ -polarized emission from the molecules, and thereby the thermalization is triggered to an SLR mode propagating along the  $y$ -axis of the lattice.

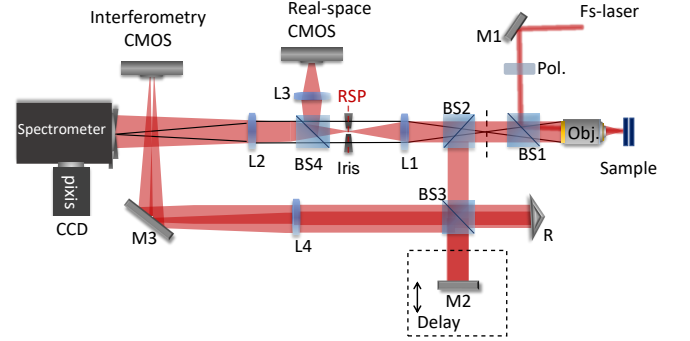


FIG. S2. Measurement setup. The sample was excited at a normal incidence by a 50 fs, 800 nm pulse. The mirror (M) 1 and beam splitter (BS) 1 were used to direct the excitation through the objective lens (Nikon 10x NA 0.3). A polarizer was used to maintain linear polarization of the excitation. The same objective was used to collect the sample luminescence, and BS2 allowed us to simultaneously perform spatial and temporal correlation measurements with a Michelson interferometer in a retroreflector configuration (Fig. 1). The Michelson interferometer accommodates a delay mirror (M2) and the retroreflector (R). The inverted and non-inverted images are focused to a CMOS camera with the  $f = 450$  mm lens (L4). To spatially crop the sample luminescence, an iris was placed at the real space image plane (RSP) after the  $f = 200$  mm tube lens, L1. The beam splitter BS4 was used to allow the collection of the real space image with L3 and the angle-resolved luminescence spectrum with L2.



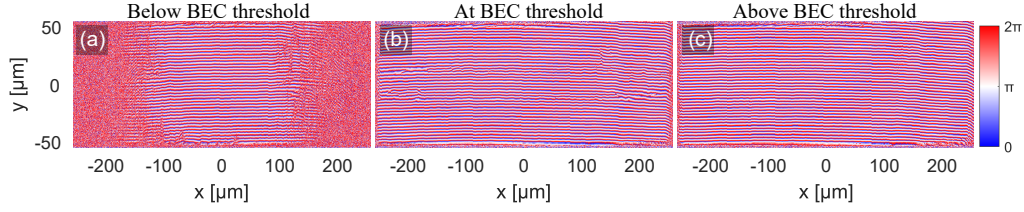


FIG. S3. Maps of the phase of the interference fringes. Phase  $\phi$  obtained by the analysis of interference fringes at three pump fluences (a) below ( $0.83 \text{ mJcm}^{-2}$ ), (b) at ( $1.66 \text{ mJcm}^{-2}$ ), and (c) above ( $3.31 \text{ mJcm}^{-2}$ ) the BEC threshold, respective to Fig. 2 of the main text.

### SPATIAL COHERENCE MEASUREMENT

Spatial and temporal coherence is measured with a Michelson interferometer in a mirror-retroreflector configuration. The measurement setup, depicted in Fig. S2, allows measuring simultaneously with the Michelson interferometer and a spectrometer in order to record the angle-resolved spectrum of the sample luminescence. Monitoring the luminescence spectrum is important to verify the stability of the condensate throughout the temporal and spatial coherence measurements.

In the Michelson interferometer, the sample luminescence is split to two arms of the interferometer with a 50/50 cube beam splitter. One of the arms is equipped with a retroreflector, while the other arm is with a flat mirror on a motorized linear stage. The location of the stage therefore sets the time delay between the two arms. The retroreflector inverts the real space image centrosymmetrically i.e. in both  $x$  and  $y$  directions of the array. The inverted and non-inverted images are overlapped at a complementary metal-oxide-semiconductor (CMOS) camera and the combined image shows interference fringes when the emission from the sample is coherent.

We measure a series of interferograms at fixed intervals around the zero time delay,  $\tau = 0$ , over approximately three cycles of light frequency oscillation. Three oscillations account for  $\sim 9 \text{ fs}$  (at  $880 \text{ nm}$ ), which is divided to 21 delay steps providing a stack of interferograms. The raw interferograms, with intensity denoted as  $I_{\text{raw}}$ , are normalized with images taken separately from each arm of the interferometer ( $I_1$  and  $I_2$ ). The interferogram with normalized intensity is  $I = (I_{\text{raw}} - I_1 - I_2) / (2\sqrt{I_1 I_2})$  [52]. The fringe contrast  $C$  is directly proportional to the absolute value of the first-order correlation function  $|g^{(1)}(\mathbf{r}, -\mathbf{r}; \tau)|$  [53]:

$$C(\mathbf{r}, \tau) = \frac{I_{\text{max}} - I_{\text{min}}}{I_{\text{max}} + I_{\text{min}}} = \frac{2\sqrt{I(\mathbf{r})I(-\mathbf{r})}}{I(\mathbf{r}) + I(-\mathbf{r})} |g^{(1)}(\mathbf{r}, -\mathbf{r}; \tau)|. \quad (\text{S1})$$

Background counts, obtained by blocking the view of the camera, are subtracted from all the images before analysis. All images taken by the CMOS camera are integrated

over 490 ms i.e. 490 excitation pulses at the 1 kHz repetition rate.

To obtain the fringe contrast, we fit a sinusoidal function,  $C \sin(\omega\tau + \phi) + C_0$ , through each pixel of the stack of normalized interferograms, providing the amplitude  $C$  and phase  $\phi$  of the fringes (see Fig. S4 for illustration). The maps of the phase  $\phi$  of the interference fringes are shown in Fig. S3. The phase reflects the ordering of correlations and can be used to confirm that the contrast has been extracted reliably by the fits. Under optimal conditions and perfectly symmetric condensate with  $I(\mathbf{r}) = I(-\mathbf{r})$ , the fringe contrast  $C$  is equal to  $|g^{(1)}(\mathbf{r}, -\mathbf{r}; \tau)|$ . This is rarely the case in experiments, hence the maximum  $|g^{(1)}| < 1$ .

When performing the experiments, the delay stage position that yields the highest fringe contrast indicates the  $\tau = 0$  position. The  $g^{(1)}(\mathbf{r}, -\mathbf{r}; \tau = 0)$  is then obtained by collecting several scans of 21 interferograms around the estimated  $\sim \tau = 0$ , and averaging the extracted  $g^{(1)}$  values of a few scans closest to the  $\tau = 0$ . The  $g^{(1)}$  in Fig. 2(g-i) and Fig. 3(a-c) is an average of three scans within a range -10 fs to 10 fs at  $\sim \tau = 0$ .

To analyze spatial correlations from the maps of  $g^{(1)}$ , we take average  $g^{(1)}(x, y)$  on a circumference with increasing diameter ( $\Delta r$ ) starting from the autocorrelation point at the center of the array. The obtained  $g^{(1)}(\Delta r)$  are fit to Gaussian, exponential, stretched exponential,

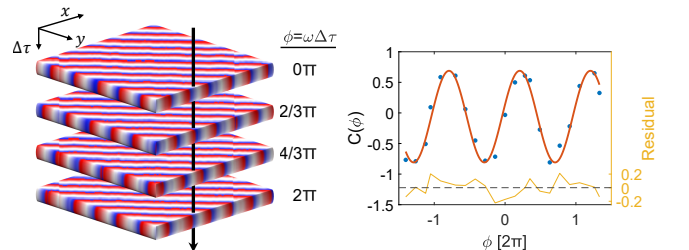


FIG. S4. Schematic illustration of the analysis of interference fringes. A sinusoidal function is fit through each pixel of the stack of 21 normalized interferograms (left panel). An example fit (red line) with 21 data points (blue dots) is shown in the right panel. Three periods of light frequency oscillation account for approximately  $\sim 9 \text{ fs}$ .

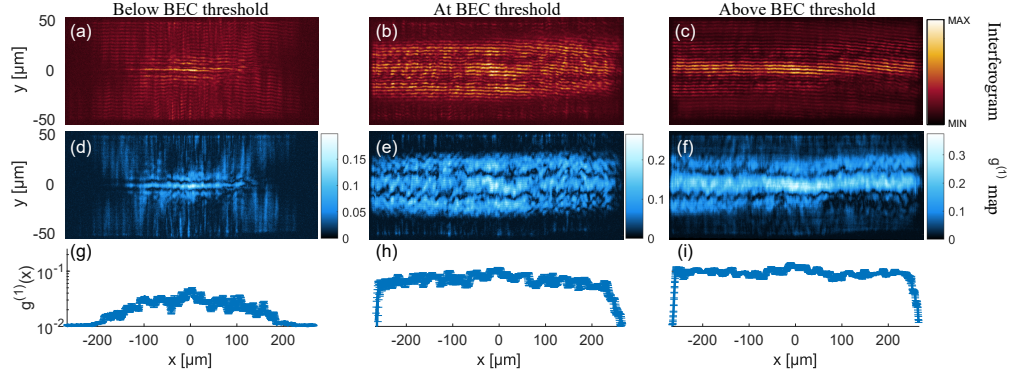


FIG. S5. Interferograms and spatial correlation maps for the thermal cloud. Interferograms at three pump fluences (a) below ( $0.83 \text{ mJcm}^{-2}$ ), (b) at ( $1.66 \text{ mJcm}^{-2}$ ), and (c) above ( $3.31 \text{ mJcm}^{-2}$ ) the BEC threshold. (d-f) Maps of  $g^{(1)}$  for the corresponding pump fluences. (g-i) Average  $g^{(1)}(x)$  taken over the  $y$ -axis in (d-f). The error bars represent the standard deviation of three measurements. Due to low number of counts, the thermal cloud data was analyzed without subtracting the background counts. Subtracting the background would lead to large negative values in the normalization procedure. Consequently, the absolute values of  $g^{(1)}$  here are not correctly normalized between  $[0, 1]$ . To separate the thermal cloud from the sample luminescence, we used two band pass filters centered at  $850 \text{ nm}$  ( $1.458 \text{ eV}$ ) with a bandwidth of  $40 \text{ nm}$ . The corresponding luminescence spectra are presented in Fig. S1.

and power-law functions, and the fit quality is assessed for each function. In addition to graphical evaluation, the fits are compared by their residuals and root-mean-square error (RMSE).

The data acquisition and analysis are demanding; the sample must remain stable throughout numerous measurements at pump fluences above the BEC threshold, and each measurement produces 21 interferograms which all contain approximately  $400 \times 2000$  pixels where the fits are performed. To reduce the computational cost, we deployed parallel computing for the non-linear least-squares fits. In turn, compared to other standard methods, such as Fourier analysis of spatial frequencies, this method provides much more robust results.

## TEMPORAL COHERENCE MEASUREMENT

For temporal coherence, interferograms were recorded over delays ranging from  $-1.25 \text{ ps}$  to  $1.25 \text{ ps}$  at fixed ( $30 \text{ fs}$ ) intervals. Here, contrary to the spatial coherence analysis, we applied a simpler method to extract the fringe contrast by fitting a sinusoidal function directly to the normalized interferograms at each delay. The fringes were analyzed from  $24 \mu\text{m}$  wide rectangles around  $x = 0$ , and the obtained  $g^{(1)}(\tau)$  was averaged over all locations in  $y$  as depicted in Fig. S7(a), see also the explanation below. The interference fringes inside the rectangular regions were fit to a sinusoidal function, which gives the amplitude of the fringes. The contrast is directly proportional to the first-order correlation function  $g^{(1)}(\tau)$ , analogous to the spatial coherence analysis. For the fits, we take the average of  $g^{(1)}(\tau)$  over negative and positive delays  $\pm\tau$  in order to get  $g^{(1)}(|\tau|)$ . The measured  $g^{(1)}(|\tau|)$  is fit to Gaussian, exponential, stretched exponential, and power-law functions. We use again the same fit range for all functions and pump fluences. In order to study long-range correlations, the SLR mode lifetime  $|\tau| = 100 \text{ fs}$  is excluded from the fits.

When extracting the temporal coherence from very small spatial regions, we observed side peaks (see Fig. S7(b) for an example) which arise from interference between counter-propagating polaritons along  $\pm y$  of the lattice (as explained above, in the main text, and in [37], the pump polarization triggers the thermalization to start along the modes where excitations propagate along the  $y$  direction). For the data used in the analysis of temporal correlation decay, we averaged over all the locations along the  $y$ -axis so that the interference peaks do not compromise the non-linear least squares fitting.

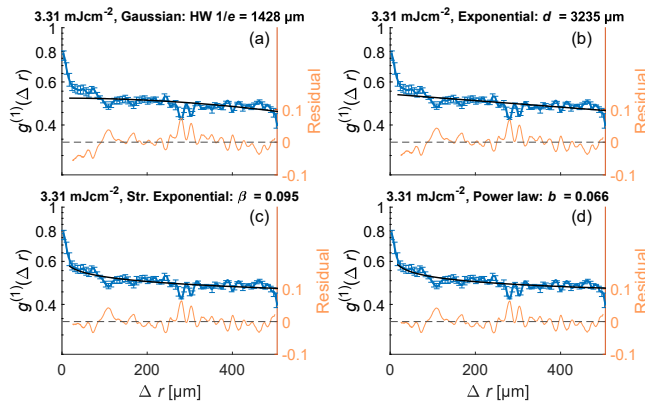


FIG. S6. Fits of the spatial correlations to all four functions. Non-linear least squares fit of measured spatial correlations at pump fluence  $3.31 \text{ mJcm}^{-2}$  to (a) Gaussian, (b) exponential, (c) stretched exponential, and (d) power-law function.

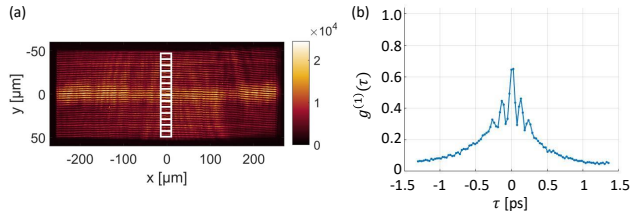


FIG. S7. Spatial locations for temporal correlation analysis. (a) The white rectangles ( $24 \times 12 \mu\text{m}$ ) illustrate the spatial locations from which the temporal correlations were extracted around  $x = 0$ . (b) An example fringe contrast data from one rectangle, displaying interference side peaks that arise from counter-propagating polaritons.